Investigation of Hohlraum Fields with Monoenergetic Proton Radiography at OMEGA

JACOB A. PEARCY,[1,*] GRAEME D. SUTCLIFFE,[1] TIMOTHY M. JOHNSON,[1] BENJAMIN L. REICHELT,[1] SKYLAR G. DANNHOFF,[1] YOUSEF LAWRENCE,[1] JOHAN FRENJE,[1] MARIA GATU-JOHNSON,[1] RICH D. PETRASSO,[1] AND CHIKANG LI[1]

[1] *Plasma Science and Fusion Center, Massachusetts Institute of Technology, 175 Albany St., Cambridge, MA 02139, USA*

[*] *pearcy@mit.edu*

Abstract: A more complete understanding of laser-driven hohlraum plasmas is critical for the continued development and improvement of ICF experiments. In these hohlraums, self-generated electric and magnetic fields can play an important role in modifying plasma properties such as heat transport; however, the strength and distribution of electromagnetic fields in such hohlraums remains largely uncertain. To explore this question, we conducted experiments at the OMEGA laser facility, using monoenergetic proton radiography to probe laser-driven vacuum hohlraums. We then utilized reconstructive methods to recover information about proton deflections. To interpret these reconstructions, a new technique for detangling the contributions of electric and magnetic fields to proton deflections was developed. This work was supported in part by the U.S. DOE, NLUF, and LLE.

1. Introduction

In the field of inertial confinement fusion, a great deal of research is focused on understanding the behavior of hohlraums, or X-ray cavities. In hohlraum (indirect drive) fusion, high-energy lasers illuminate the walls of the cavity to produce a uniform X-ray bath, which compresses a fuel capsule to fusion-relevant temperatures and densities. Given their importance to the fusion initiative, a detailed understanding of hohlraum physics is critical. Prior work [1–3] has indicated that self-generated electromagnetic fields can substantially alter the transport properties of the hohlraum plasma and impact target performance. However, detailed information about the fields present in hohlraums has proven difficult to obtain experimentally. To that end, we seek in this work to develop techniques to better understand the strength and distribution of electric and magnetic fields within laser-driven vacuum hohlraums, using high-energy monoenergetic proton radiography as our primary probing diagnostic.

Techniques for reconstructing path-integrated electromagnetic fields from proton radiography [4–6] have recently begun to move to the forefront of radiography analysis. Given certain assumptions (discussed in Section 2.2.1), such reconstruction algorithms can recover from a given proton image and initial flux distribution a "perpendicular deflection field" which depends on the electric and magnetic fields encountered by the protons in the subject plasma. Interpretation of the results of such algorithms is an important problem in the analysis of proton radiography. Prior work with results depending on the output of reconstruction algorithms (for example, [7–9]) have investigated experimental geometries where assuming deflections are dominated by magnetic fields is justified. However, in other experiments (such as the hohlraums considered in this manuscript) neither purely electric nor purely magnetic field deflections can explain observations. Here, we describe one approach we have developed for attempting to detangle the contributions from both fields.

2. Methods

2.1. Experimental Design

The experiments performed to investigate these effects were conducted at the University of Rochester Laboratory for Laser Energetics' OMEGA Laser Facility. The experimental subject is a gold hohlraum with 100% laser-entrance-hole, i.e. a gold "can," containing neither a fuel capsule nor a gas fill (i.e., a "vacuum hohlraum"). The hohlraums in this experiment had an outer diameter of 2.4 mm, and a length of 4 mm. The hohlraum was driven axisymmetrically from either the left side of the hohlraum with 10 beams of laser drive, or from the right side of the hohlraum with 9 beams of laser drive[1], with each beam having a 1 ns laser pulse and an energy of 500 joules per beam delivering energy to a laser spot size of roughly 358 μm (standard SG-5 phase plates). To diagnose the hohlraum, a standard backlighter capsule for monoenergetic proton radiography [10] was used. The backlighter consisted of a 2.0 micron thick, 420 micron outer diameter SiO_2 spherical shell filled with a 50:50 (number density) mixture of deuterium and helium-3 gas at 18.0 atm (henceforth referred to as a "D^3He backlighter"), was positioned 1 cm away from the hohlraum, and was driven with 40 laser beams also with 1.0 ns pulse and energy of 500 joules per beam. The experimental setup is shown in cartoon form in Figure 1.

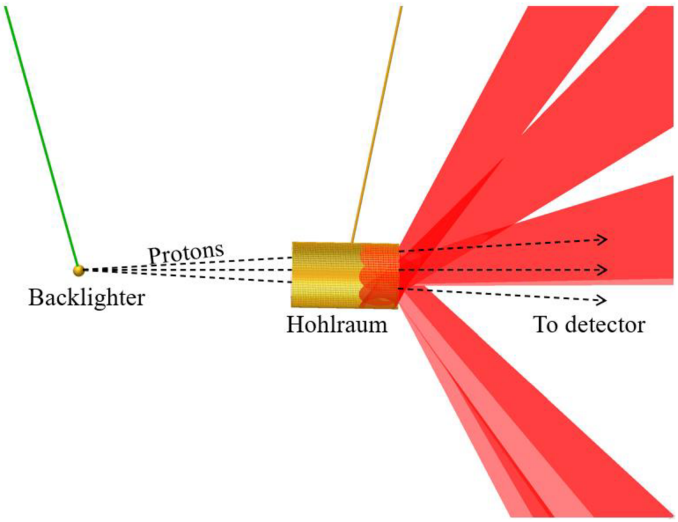

Fig. 1. Cartoon of the experimental setup, showing the capsule backlighter suspended by a stalk at left, and the hohlraum suspended by a stalk on the right. Dotted arrows schematically represent proton trajectories from the backlighter, while the red shaded areas denote the 9 drive laser beams on the hohlraum. For clarity, the 40 drive beams aimed at the backlighter are not pictured.

The D^3He backlighter produces nearly monoenergetic protons at two distinct energies; 3.0 MeV protons from deuterium-deuterium fusion ("DD protons") and 14.7 MeV protons from deuterium-helium 3 fusion ("D^3He protons"). By varying the relative timing delay between backlighter beams and hohlraum beams, the structure of electromagnetic fields in the hohlraum was probed at different sample times.

In order to measure the flux of protons, a solid-state detector composed of the plastic material Columbia Resin No. 39 (henceforth "CR-39") was used [11]. Ions impacting the surface of the CR-39 deposit their energy and leave tracks of chemical damage; submerging of the CR-39 in a

[1]The one beam left over was reserved as a probe beam for Thomson scattering measurements not discussed in this manuscript.

solution of NaOH then preferentially etches areas where such damage has occurred, expanding the diameter of those tracks. By scanning the etched CR-39 under a microscope, individual proton tracks (and therefore detailed information about the proton flux) are ascertained. In this experiment, the CR-39 detector consisted of two 10 cm by 10 cm pieces of CR-39 positioned 27 cm away from the hohlraum. In order to obtain information about both proton species, the two pieces of CR-39 are sandwiched between specifically chosen metal filtering to range down protons into an appropriate energy range. Two representative radiographs from a shot on this experimental campaign are shown in Figure 2.

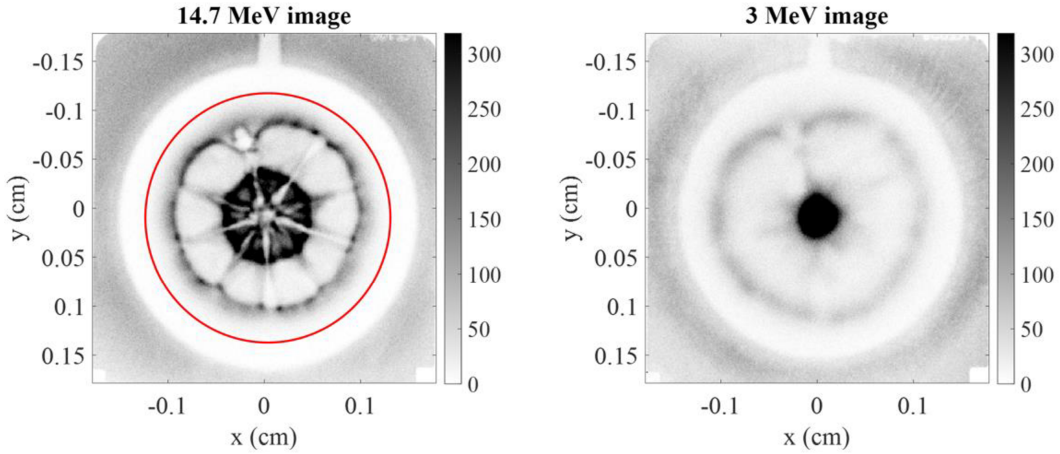

Fig. 2. The processed proton radiography images of the vacuum hohlraum; the image on the left was formed by 14.7 MeV D^3He protons, while the image on the right was formed by 3 MeV DD protons. In these images, the 14.7 MeV protons sampled the hohlraum fields ~1.4 ns after the start of the hohlraum drive. The ninefold symmetry of these radiographs reflects the 9-beam axisymmetric laser drive on the hohlraum, while the dark central feature indicates a focusing of protons towards the center of the image. These images will be used to demonstrate the novel methods for electromagnetic field discrimination from deflection field reconstruction.

2.2. Analysis

2.2.1. Deflection Field Reconstruction

In order to recover information about the electromagnetic fields deflecting protons to produce the observed radiographs, reconstructive techniques developed by A. Bott (as described in [4]) were utilized. The reconstruction hinges on the fact that the flux of protons at the detector is directly related to the angular deflection that the protons experience as they travel from the source to the screen. This relationship is encoded in the Kugland image flux relation [12, 13]

$$\Psi\left(\vec{x}_\perp^{(s)}\right) = \frac{\Psi_0}{\det\left(\nabla_0\left(\vec{x}_\perp^{(s)}\right)\right)} \tag{1}$$

where Ψ is the flux of the protons recorded at the detector, Ψ_0 is what the proton flux at the detector would have been in the absence of any field deflections, $\vec{x}_\perp^{(s)}$ are the perpendicular coordinates of protons at the detector screen, and ∇_0 is the gradient taken with respect to the perpendicular coordinates of protons prior to their deflection by the subject fields (see Fig. 3 for a pictoral representation of these quantities).

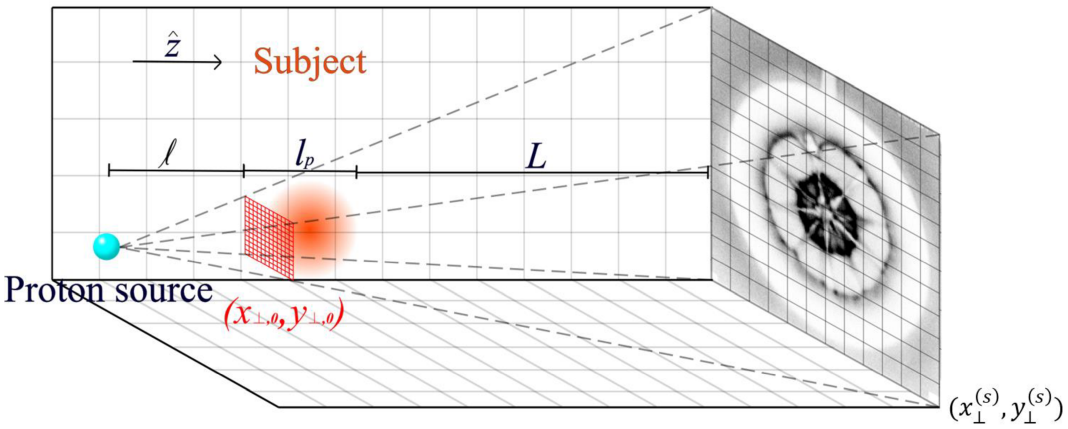

Fig. 3. A cartoon showing the approximate geometry of the experiment (dimensions of objects and lengths are not drawn to scale). The $\hat{z}$ direction points horizontally to the right of the image. At the far left is a cyan sphere representing the capsule-type proton source; from it, dotted lines representing proton trajectories emanate. The protons traverse a distance ℓ before encountering the orange subject plasma, which has perpendicular extent $l_{\perp,p}$; their positions before being disturbed by the plasma conditions are $\vec{x}_{\perp,0} = (x_{\perp,0}, y_{\perp,0})$. They interact with the subject plasma over a distance l_p before continuing to propagate to the screen over a distance of L; their coordinates at the screen are $\vec{x}_\perp^{(s)} = (x_\perp^{(s)}, y_\perp^{(s)})$.

The connection to the deflecting fields is made by relating the screen coordinates $\vec{x}_\perp^{(s)}$ to the unperturbed coordinates $\vec{x}_{\perp,0}$ by a combination of magnification and perpendicular deflection due to electromagnetic fields (neglecting plasma scattering effects);

$$\vec{x}_\perp^{(s)}(\vec{x}_{\perp,0}) = \frac{L+\ell}{\ell}\vec{x}_{\perp,0} + \frac{L}{v}\vec{w}(\vec{x}_{\perp,0}) \tag{2}$$

where ℓ and L are the source and screen distances (labelled in Fig 3), v is the velocity of the probing proton, and $\vec{w}$ is the perpendicular velocity deflection field (equivalent to the angular deflection multiplied by the probe particle velocity) determined by the path-integrated electric and magnetic fields;

$$\vec{w} = \frac{q}{mc}\int_\ell \left(\hat{z}\times\vec{B}\right)dz + \frac{q}{\sqrt{2mW}}\int_\ell \vec{E}\,dz \equiv \vec{w}_B + \vec{w}_E \tag{3}$$

Here q is the charge of the probing particle, m the particle's mass, c the speed of light, $\hat{z}$ the direction of probing particle motion, $\vec{B}$ the encountered magnetic field, W the particle's kinetic energy, and $\vec{E}$ the encountered electric field, and $\vec{w}_B$ and $\vec{w}_E$ are defined here to be the contributions to the deflection field from magnetic and electric fields, respectively. As described in [4], these relations can be combined together to construct a log-parabolic Monge-Ampere equation, which is then solved numerically using finite difference methods. Then, given these relations and a routine for solving the resulting Monge-Ampere equation, by measuring the flux of protons at the detector screen Ψ, then inferring or assuming an initial proton flux Ψ_0, we can "reconstruct" the perpendicular velocity deflection field $\vec{w}$ that resulted in a particular proton image.

Here it is important to note that the reconstruction of the perpendicular deflection field using the equations in this section requires a certain number of assumptions be made about the trajectories

of the protons as they traverse the subject plasma. Though these assumptions are discussed in detail in [4], summarize here the important points.

First, there are important orderings between length scales in the problem that must be obeyed for the equations to be valid. We require that: $l_{\perp,p}$, the perpendicular dimension of the subject plasma, is much smaller than L; and that l_p, the dimension of the plasma along the probing dimension, is much smaller than both ℓ and L. These length assumptions are well-satisfied by the conditions of our experiment.

The second assumption (which is more problematic when it comes to actual implementation) inherent to the equations of reconstruction is that proton trajectories do not intersect each other between the proton source and the detector screen. One can imagine proton trajectories moving through the system as a cluster of proton beamlets, which can be moved relative to each other by electromagnetic fields but cannot be allowed to cross if the problem is to remain soluble. If the tracks do cross each other, the mapping between initial proton coordinates and final proton coordinates is no longer injective, and the Kugland image flux relation cannot be used as the quantity in the denominator becomes singular [12]. In such a situation, the proton flux should formally become infinite at the detector screen at a location referred to as a "caustic," though in practice the proton flux remains finite due to the finite resolution of the diagnostic. Visual identification of caustics in a proton image is therefore important, as if they are present then numerical reconstruction cannot be performed; however, due to the finite resolution of the radiography it is generally a difficult task to definitively identify caustics, particularly in cases where only a single image is obtained. When two or more proton species are used for imaging, as with the D^3He backlighter, comparison of multiple images with different probing energies can aid in the identification of caustics because dark caustic features in a high-energy radiograph tend to be broadened and more exaggerated in a lower-energy radiograph. For this reason, for example, we interpret the dark central feature in the radiographs of Fig. 2 to be plausibly non-caustic; its size decreases in the image produced by lower energy protons rather than increases.

The requirement that no caustics be present has critical implications for the selection of which energy of proton will be used for numerical reconstruction, which in turn has an important bearing on the determination of electric and magnetic fields from the perpendicular velocity deflection.

2.2.2. Field Discrimination

The primary focus of this work was the development of a new technique to recover information about the electric and magnetic fields separately from the perpendicular deflection field; as Eq. 3 makes clear, the deflection field is a derived quantity which depends on both fields. As a single proton image yields only a single perpendicular deflection field, unique identification of both electric and magnetic fields is not possible. However, if multiple images are available, it is in principle possible to recover information about both fields [13].

Because the D^3He backlighter produces both DD and D^3He protons simultaneously which sample the subject plasma at similar times (separated by the travel time difference between the two proton species), one can theoretically separately reconstruct each image, and the two deflection fields could be combined to algebraically recover both electric and magnetic fields because of the different energy dependence for deflections from each field type. However, the no-crossing condition for proton tracks becomes a significant limiter for the lower energy DD proton; because lower energy protons are deflected farther by strong field gradients than more energetic ones, the DD image is more likely to exhibit caustics. Furthermore, because Coulomb scattering effects in the plasma are also more significant for lower energy protons, given a dense subject plasma the DD image is likely to be significantly blurred, making visual identification of caustic features very difficult. If a DD proton image containing caustics were mistakenly reconstructed, the using the resulting deflection field to calculate electromagnetic field strengths

would yield incorrect results.

Therefore, it is important from an experimental perspective to develop techniques for inferring information about electric and magnetic fields from a single high-energy proton radiography reconstruction; the 14.7 MeV D^3He proton produces images which are less likely to contain caustics, and which have much finer spatial resolution, making identification of possible caustics significantly easier.

The technique developed for this work involves reconstructing a D^3He radiograph to recover a perpendicular deflection field, then making an assumption about the contributions of the electromagnetic fields to the deflection field which depends on the value of at least one parameter. The fields derived from this assumption can then be used to construct a resulting deflection field for the DD proton, and then produce a synthetic DD proton radiograph which can be visually and numerically compared to the actual DD proton data (as the forward process of going from a deflection field to a radiograph does not suffer the same ambiguity caused by caustics in the inverse problem). The parameters associated with the field assumption can then be varied until as close a match as possible is obtained. If a close match is realized, then the fields which produced it are taken to be reasonably representative of the true fields in the experiment.

One particularly simple example of the kind of field assumption one might make is that electric and magnetic fields deflect particles in the same direction throughout the image, with some fraction $f < 1$ (the "field fraction") of the deflection fields caused by electric fields and the remainder caused by magnetic fields; that is, $\vec{w}_E = f\vec{w}$, and $\vec{w}_B = (1-f)\vec{w}$, with $\vec{w} = \vec{w}_E + \vec{w}_B$ (throughout, a $\vec{w}$ without explanatory superscript is taken to be the deflection field for the D^3He proton, while the DD quantity where mentioned will be labelled $\vec{w}^{\mathrm{DD}}$). This assumption leaves the field fraction f as the single free parameter to vary to attempt to forward-match the DD proton image.

Although this technique works well for synthetic data specifically tailored to satisfy the field fraction assumption, in radiography from actual experiments a global fraction f cannot reproduce features of the images in all regions. The next step we take here, then, is to divide the radiographs into separate regions R_i where different physics may be dominant, each with different field fractions f_i; then by varying each f_i independently, convincing matches to the experimental data can be obtained.

3. Demonstration of Techniques

In this section, we show a demonstration of the techniques described in the previous section on a representative shot from the OMEGA experiment. To begin, we start with the 14.7 MeV radiograph shown in Figure 2. This is the image on which reconstruction will be performed.

The first step is to select the region of the image in which we would like to perform the reconstruction. Recalling that the equations governing the reconstruction process require that proton deflections be dominated by electromagnetic field effects (rather than scattering or stopping in matter), it is necessary to select a region of the image where the proton source is not obscured by the material of the hohlraum wall itself (else, the lack of flux in those regions would be mistakenly identified as strong electromagnetic fields). In the radiograph, this is identified by the white rings of zero proton flux; thus, we select a circular region near the center of the image to perform reconstruction on, denoted in the figure by the red circle in the 14.7 MeV image (though the identification here is visual, in later experimental campaigns the region of hohlraum obstruction will be exactly identified by using image plates sensitive to X-rays – which are also obstructed by the hohlraum wall – in the proton radiography detector stack). To account for the non-rectangular boundary of the region of interest, we employ the "shadow flux" method described in [4]: the region exterior to the circular boundary is filled with an artificial "shadow flux" value which is the same in both the initial flux distribution and the measured radiograph. Then the entire rectangular image is reconstructed as usual. Although this is only an approximate

technique, as the authors of [4] note conservation of particle number in the reconstruction and exterior regions implies that the recovered deflection fields are close to the true deflection fields. Exact treatment of arbitrary boundary conditions in different radiography geometries is a challenge for future work.

In order to infer the initial proton flux (a quantity which is important to the reconstruction procedure but not simultaneously measurable during a shot), we utilize a low-pass spatial filter to remove small-scale fluctuations in proton fluence, as these would be the features which arise from electromagnetic deflections. The remaining large-scale variation is attributed to nonuniform initial proton flux. For capsule-type backlighters, null radiography displays features with significant ($\gtrsim 30\%$) flux variation with sizes on the order of the entire image [14, 15], so choosing a cutoff wavelength which is near the scale of the object being imaged tends to produce realistic initial flux distributions with characteristics consistent with the measured distribution of protons in null radiography shots.

Having selected the region of interest and inferred this initial flux, the reconstruction can be carried out and a perpendicular deflection field can be recovered; a map of the deflection field magnitude for this 14.7 MeV proton image is shown in Figure 4.

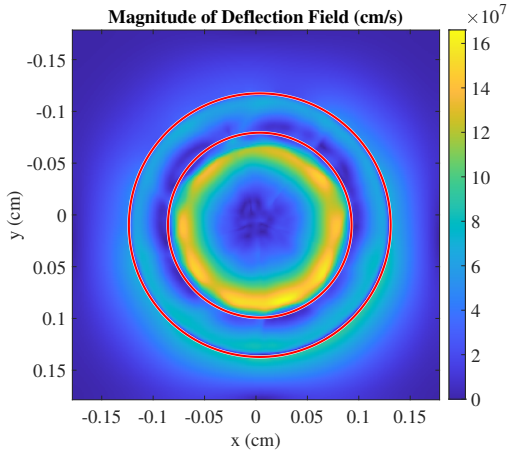

Fig. 4. A heat map showing the magnitude of the perpendicular deflection $|\vec{w}|$ field as inferred from the 14.7 MeV proton image. The two red rings denote the boundary between regions R_i selected for different field fractions and the outer boundary of the reconstruction region, respectively.

The deflection field is then divided into two or more regions with different field fraction breakdowns. In this and other hohlraum examples, we use two regions R_i which are concentric circles; a region R_1 near the center of the hohlraum, and a region R_2 nearer the hohlraum wall. Each subdivision is then assigned a range of initial field fractions (in this case, four evenly spaced between $f_i = 0$ and $f_i = 1$), which can be later refined as more information about the problem is gained. To avoid numerical issues and an unphysical singular jump in fraction between the two regions, a thin (10 pixel) smoothing region between is also assigned wherein the field fraction transitions linearly from one to the other. Representative maps of the field fraction breakdowns for visualization purposes are provided in Figure 5.

From each of these different regional field breakdowns, candidate path-integrated electric and magnetic field distributions are inferred. To be clear, given the constraints of the problem each of these electromagnetic distributions will exactly reproduce the input D^3He image, so at this stage in the process no information about discriminating between the different distributions is possible.

In order to discriminate, we utilize the DD proton image as a point of comparison. Each

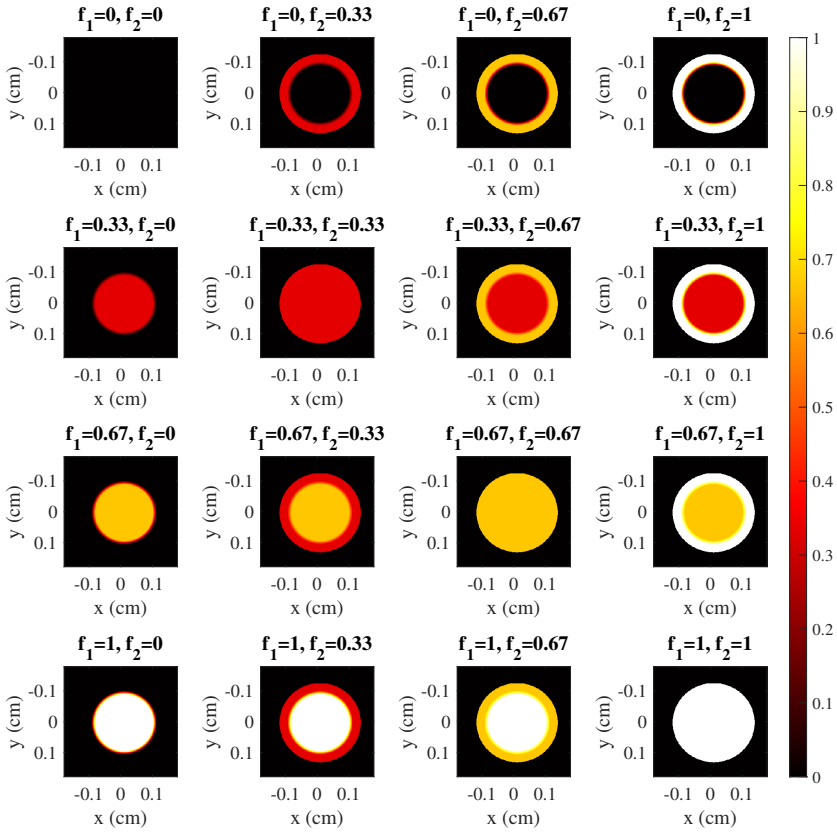

Fig. 5. Color maps of the field fraction breakdowns assigned to each image; the color bar is common to each map. In the figure titles, f_1 is the field fraction in the inner region R_1, while f_2 is the field fraction in the outer region R_2. Information outside the reconstruction region is ignored.

different field distribution is used to generate a corresponding DD proton deflection field $\vec{w}^{\mathrm{DD}}$ (not pictured here), which can then be used to calculate a synthetic DD proton image for comparison with the DD data (displayed as the second panel in Figure 2). Because electric and magnetic fields deflect probing particles to different degrees depending on the particle energy, while each field configuration reproduces the D^3He image exactly they each produce a different DD proton image. The synthetic DD proton images are then artificially blurred to simulate source size and plasma scattering effects before comparing them to the DD data; blurred radiographs produced from the field fractions in Fig. 5 are shown in Fig. 6.

4. Discussion and Results

As is clear from the images, significant morphological differences in each region are apparent as each field fraction varies from 0 to 1. Because electric fields cause angular deflections with $1/W$ dependence while magnetic fields cause angular deflections with $1/\sqrt{W}$ dependence (see Eq. (3)), the differences between the DD and D^3He images (and the features of the synthetic data in general) become progressively more exaggerated as the field fraction becomes more and

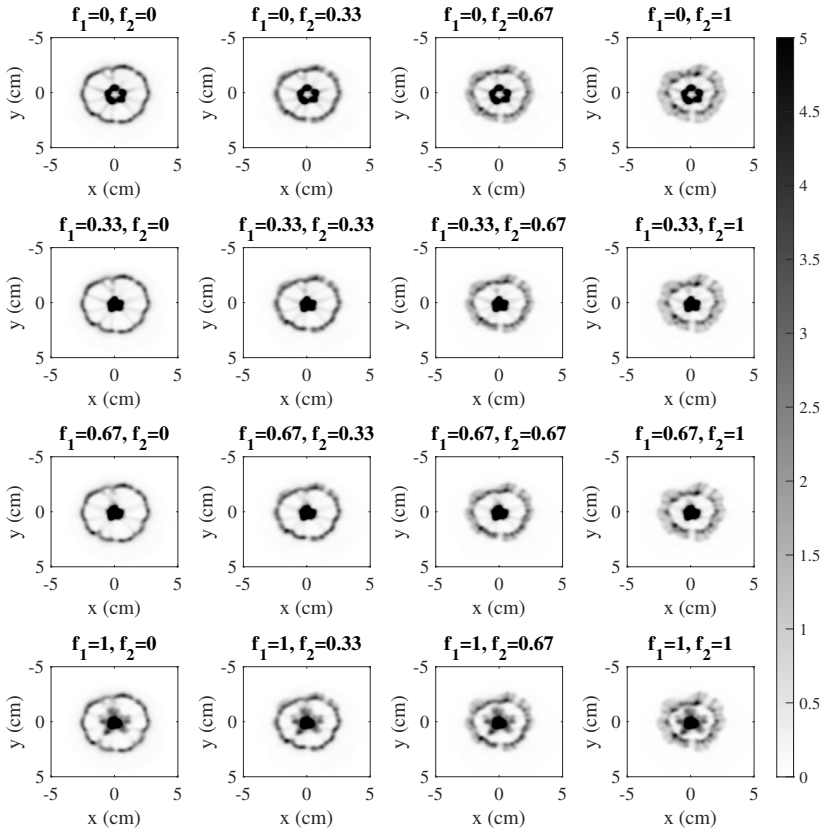

Fig. 6. Synthetic DD proton images produced from the deflection fields calculated from the electromagnetic field configurations implied by the field fraction breakdowns in Figure 5. Both the inner and outer regions show clear variations in feature sizes and locations with field fraction which can be used as comparisons with the true DD proton data in Figure 2. These images have had a Gaussian blur applied in post-processing to simulate plasma scattering conditions present in the actual DD proton data. The color bar denotes proton flux relative to the mean flux in each image.

more electric. In the center region, the central feature transitions from a ring qualitatively similar to that displayed in the D^3He radiograph at the most magnetic field fractions, to a condensed dark spot at intermediate fractions, to a clearly caustic feature where protons from different parts of the image have crossed paths and been deposited nonlocally at the most electric fraction. In the outer region, the dark ring near the hohlraum wall varies in size from small and localized at mostly magnetic fractions to very broad at mostly electric fractions where caustics have formed. The clear formation of caustic features in both the inner at outer regions at high electric field proportion emphasize the necessity of not using the DD radiograph for quantitative reconstruction when strong fields are thought to be present. These features allow a quick qualitative judgment of which combination of field fractions best reproduces the DD data; in this case, it is clear that the central feature is best reproduced by an intermediate value of f_1 and the outer feature by a low value of f_2.

In order to quantitatively assess which combination best fits the data, as a simple metric we

utilize an averaged radial profile. For each synthetic radiograph we compare its radial profile to that of the DD proton data, and calculate residuals to quantify how different the two profiles are. The summed square of the residuals is plotted in Fig. 7A). A best fit is clearly visible, with direct comparison of lineouts between the best fit and the DD proton data shown in Fig. 7B).

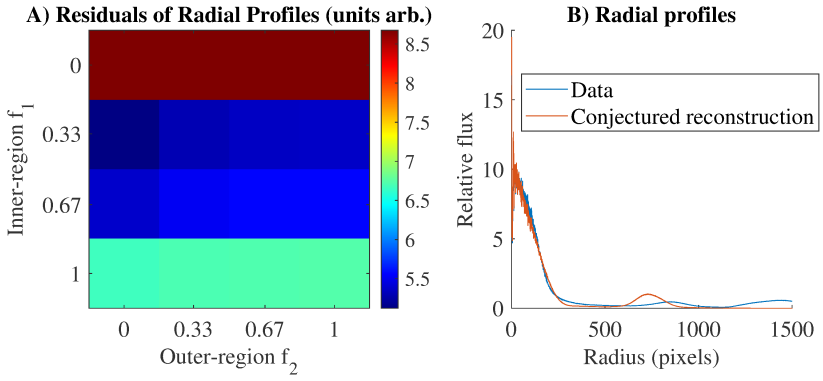

Fig. 7. A) Matrix of field fraction breakdowns showing a colors which quantify the residual values between a radial profile of the conjectured reconstruction and a radial profile of the actual DD data. The units on the color axis are arbitrary. The fit with lowest residual is clearly visible as the dark blue square. B) Direct comparison of radial lineouts between the best fit and the DD proton data. Note that in the conjectured reconstruction, pixel values outside the outer radius of reconstruction are artificially zeroed.

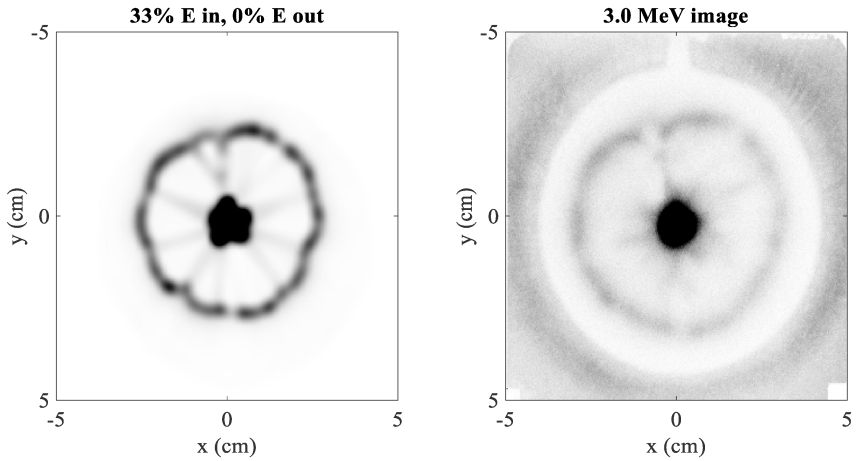

Fig. 8. Direct side-by-side visual comparison of the calculated best-fit synthetic DD proton image (on the left) and the DD proton data (on the right). Although not a perfect reproduction, gross features common to both are clearly identifiable, suggesting that the fit is reasonable.

A direct comparison between the calculated best-fit synthetic image and the DD proton data is shown in Fig. 8. Note that in the synthetic image, all flux from the region outside the region of

reconstruction is ignored. As can be seen, many features of the data are able to be successfully reproduced by our technique, including the size and approximate shape of the central feature, as well as noticeable perturbations in the outer ring (such as the gap near 6:00, and the blob-like feature between 11:00 and 12:00). The location of spokes emanating from the central region also match reasonably well, although their radial extent is not reproduced.

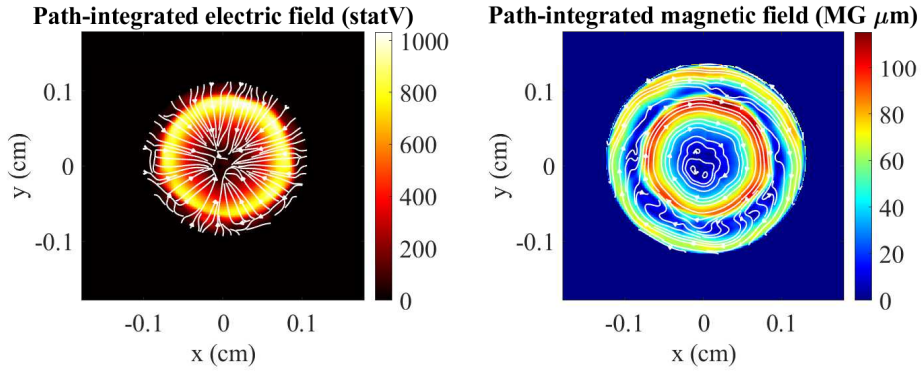

Fig. 9. The inferred path-integrated electric and magnetic fields taken from the best-fit field fraction breakdown. All quantities quoted are integrated along the $\hat{z}$-direction of proton propagation.

Finally, from the best-fit field fraction breakdown, we then recover the inferred path-integrated electric and magnetic fields experienced by the probing protons, shown in Fig. 9. Note that these results are still not direct field strengths but instead are integrated along the direction of proton propagation (as is necessarily the case in proton radiography measurements) – further assumptions about the proton trajectories and the structure of the fields experienced by the protons are necessary to recover bare field strengths. In particular, places where protons alternately traverse regions with oppositely directed fields can experience zero (or otherwise reduced) net deflection (as has been experimentally confirmed for side-on radiography of laser-produced plasma bubbles [16]); as we anticipate the presence of this type of geometry in this experiment, naive interpretation of the path-integrated fields is likely misleading.

To reiterate, these path-integrated fields exactly reproduce the data D^3He proton radiograph, and produce the synthetic DD radiograph in Fig. 8 which compares quite favorably to the actual data, suggesting that they are a reasonable representation of the true path-integrated fields in the experiment.

5. Conclusion and Future Avenues

In conclusion, we have developed a new technique for interpreting reconstructions of proton radiographs that allows recovery of both electric and magnetic field information from a single high-energy proton radiograph, given the presence of a low-energy proton image to use for comparison and verification purposes. This technique (much like other methods for interpreting the output of proton radiography reconstruction algorithms) is still in its nascent stages, and many opportunities for refinement and improvement are apparent. One of the most obvious improvements would be the relaxation of the assumption that electric and magnetic fields deflect protons in the same direction in each region; though this represents a wide parameter space to explore, work is underway to make improvements along this line. Another clear path forward is increasing the number of regions included in the discrimination procedure, ideally aided by computer simulations of the experiments in question to provide more definitive insight into which

regions are dominated by different physics – this is particularly important in experiments with more complex geometries than the hohlraums. Efforts along these lines are likewise underway.

Another exciting improvement to the interpretation of proton radiography comes with the recent development of the tri-particle fusion backlighter [17]. This technology allows for a simultaneous third radiograph to be obtained from the 9.5 MeV T^3He deuteron. This third particle is characteristically more similar to the 14.7 MeV proton than the 3 MeV proton, resurrecting the possibility of using two near-simultaneous radiographs to fully depart from assumptions about the field geometries and reconstruct both fields simultaneously. Analysis of triparticle data from hohlraums is another avenue actively being pursued in this field.

That said, these results represent an important step forward in the interpretation of proton radiography, and pave the way for exciting developments in the future.

6. Backmatter

Acknowledgments. Portions of this work were presented at the Optica Imaging Congress in 2023, paper ID JTu4A.11

In the process of this research, J. Pearcy was the primary developer of the techniques for interpreting radiograph reconstructions, and was primarily responsible for the preparation of this manuscript. J. Pearcy and C. K. Li conducted the OMEGA experiments and provided the dataset. G. Sutcliffe, T. Johnson, B. Reichelt, S. Dannhoff, and Y. Lawrence were also deeply involved in interpreting the results of the OMEGA hohlraum experiments, and making improvements to the numerical methods utilized in reconstructing the proton data. J. Frenje, M. Gatu Johnson, and R. Petrasso provided support and valuable scientific insight in the course of the research. All listed coauthors provided guidance in the preparation of this manuscript.

This work was supported in part by US DOE/NNSA CoE contract DE-NA0003868, US DoE/NNSA Award No. DE-NA0003856, DOE/NNSA HEDLP contract DE-NA0004129, and NLUF contract DE-NA0003938

Disclosures. The authors declare no conflicts of interest.

Data Availability Statement. Data underlying the results presented in this paper are not publicly available at this time but may be obtained from the authors upon reasonable request.

References

1. S. H. Glenzer, W. E. Alley, K. G. Estabrook, J. S. De Groot, M. G. Haines, J. H. Hammer, J.-P. Jadaud, B. J. MacGowan, J. D. Moody, W. Rozmus, L. J. Suter, T. L. Weiland, and E. A. Williams. Thomson scattering from laser plasmas. *Physics of Plasmas*, 6(5):2117–2128 (1999). doi:10.1063/1.873499.
2. W. A. Farmer, J. M. Koning, D. J. Strozzi, D. E. Hinkel, L. F. Berzak Hopkins, O. S. Jones, and M. D. Rosen. Simulation of self-generated magnetic fields in an inertial fusion hohlraum environment. *Physics of Plasmas*, 24(5):052703 (2017). doi:10.1063/1.4983140.
3. J. D. Sadler, C. A. Walsh, Y. Zhou, and H. Li. Role of self-generated magnetic fields in the inertial fusion ignition threshold. *Physics of Plasmas*, 29(7):072701 (2022). doi:10.1063/5.0091529.
4. A. F. A. Bott, C. Graziani, P. Tzeferacos, T. G. White, D. Q. Lamb, G. Gregori, and A. A. Schekochihin. Proton imaging of stochastic magnetic fields. *Journal of Plasma Physics*, 83(6):905830614 (2017). doi:10.1017/S0022377817000939.
5. M. F. Kasim, L. Ceurvorst, N. Ratan, J. Sadler, N. Chen, A. Sävert, R. Trines, R. Bingham, P. N. Burrows, M. C. Kaluza, and P. Norreys. Quantitative shadowgraphy and proton radiography for large intensity modulations. *Physical Review E*, 95(2):023306 (2017). doi:10.1103/PhysRevE.95.023306.
6. N. F. Y. Chen, M. F. Kasim, L. Ceurvorst, N. Ratan, J. Sadler, M. C. Levy, R. Trines, R. Bingham, and P. Norreys. Machine learning applied to proton radiography of high-energy-density plasmas. *Physical Review E*, 95(4):043305 (2017). doi:10.1103/PhysRevE.95.043305.
7. A. F. A. Bott, P. Tzeferacos, L. Chen, *et al.* Time-resolved turbulent dynamo in a laser plasma. *Proceedings of the National Academy of Sciences*, 118(11):e2015729118 (2021). doi:10.1073/pnas.2015729118.
8. A. Bott, L. Chen, G. Boutoux, T. Caillaud, A. Duval, M. Koenig, B. Khiar, I. Lantuéjoul, L. Le-Deroff, B. Reville, R. Rosch, D. Ryu, C. Spindloe, B. Vauzour, B. Villette, A. Schekochihin, D. Lamb, P. Tzeferacos, G. Gregori, and A. Casner. Inefficient Magnetic-Field Amplification in Supersonic Laser-Plasma Turbulence. *Physical Review Letters*, 127(17):175002 (2021). doi:10.1103/PhysRevLett.127.175002.
9. P. Tzeferacos, A. Rigby, A. F. A. Bott, *et al.* Laboratory evidence of dynamo amplification of magnetic fields in a turbulent plasma. *Nature Communications*, 9(1):591 (2018). doi:10.1038/s41467-018-02953-2.
10. C. K. Li, F. H. Séguin, J. A. Frenje, J. R. Rygg, R. D. Petrasso, R. P. J. Town, P. A. Amendt, S. P. Hatchett, O. L. Landen, A. J. Mackinnon, P. K. Patel, V. A. Smalyuk, J. P. Knauer, T. C. Sangster, and C. Stoeckl. Monoenergetic

proton backlighter for measuring E and B fields and for radiographing implosions and high-energy density plasmas (invited). *Review of Scientific Instruments*, 77(10):10E725 (2006). doi:10.1063/1.2228252.

11. F. H. Séguin, J. A. Frenje, C. K. Li, D. G. Hicks, S. Kurebayashi, J. R. Rygg, B.-E. Schwartz, R. D. Petrasso, S. Roberts, J. M. Soures, D. D. Meyerhofer, T. C. Sangster, J. P. Knauer, C. Sorce, V. Y. Glebov, C. Stoeckl, T. W. Phillips, R. J. Leeper, K. Fletcher, and S. Padalino. Spectrometry of charged particles from inertial-confinement-fusion plasmas. *Review of Scientific Instruments*, 74(2):975–995 (2003). doi:10.1063/1.1518141.
12. N. L. Kugland, D. D. Ryutov, C. Plechaty, J. S. Ross, and H.-S. Park. Invited Article: Relation between electric and magnetic field structures and their proton-beam images. *Review of Scientific Instruments*, 83(10):101301 (2012). doi:10.1063/1.4750234.
13. D. B. Schaeffer, A. F. Bott, M. Borghesi, K. A. Flippo, W. Fox, J. Fuchs, C. Li, F. H. Séguin, H.-S. Park, P. Tzeferacos, and L. Willingale. Proton imaging of high-energy-density laboratory plasmas. *Reviews of Modern Physics*, 95(4):045007 (2023). doi:10.1103/RevModPhys.95.045007.
14. M. J.-E. Manuel, A. B. Zylstra, H. G. Rinderknecht, D. T. Casey, M. J. Rosenberg, N. Sinenian, C. K. Li, J. A. Frenje, F. H. Séguin, and R. D. Petrasso. Source characterization and modeling development for monoenergetic-proton radiography experiments on OMEGA. *Review of Scientific Instruments*, 83(6):063506 (2012). doi:10.1063/1.4730336.
15. F. H. Séguin, C. K. Li, J. A. Frenje, S. Kurebayashi, R. D. Petrasso, F. J. Marshall, D. D. Meyerhofer, J. M. Soures, T. C. Sangster, C. Stoeckl, J. A. Delettrez, P. B. Radha, V. A. Smalyuk, and S. Roberts. Measurements of ρR asymmetries at burn time in inertial-confinement-fusion capsules. *Physics of Plasmas*, 9(8):3558–3566 (2002). doi:10.1063/1.1492806.
16. G. D. Sutcliffe, P. J. Adrian, J. A. Pearcy, T. M. Johnson, J. Kunimune, B. Pollock, J. D. Moody, N. F. Loureiro, and C. K. Li. Observation of electromagnetic filamentary structures produced by the Weibel instability in laser-driven plasmas (2022). ArXiv:2209.02565 [physics].
17. G. Sutcliffe, P. Adrian, J. Pearcy, T. Johnson, N. Kabadi, S. Haque, C. Parker, B. Lahmann, J. Frenje, M. Gatu-Johnson, H. Sio, F. Séguin, B. Pollock, J. Moody, V. Glebov, R. Janezic, M. Koch, R. Petrasso, and C. Li. A new tri-particle backlighter for high-energy-density plasmas (invited). *Review of Scientific Instruments*, 92(6):063524 (2021). doi:10.1063/5.0043845.